Advanced Electronic Materials

ADVANCED ELECTRONIC MATERIALS Open Access

www.advelectronicmat.de

RESEARCH ARTICLE OPEN ACCESS

Incorporation of Extrinsic Alkali Cations Modulates Ion Migration and Hysteresis in Lateral $MAPbBr_3$ Devices

Hongxin Yuan[1] | Yahong Pu[2] | Darrell Jun Jie Tay[1] | Si En Ng Timothy[1] | Yanfang Zhang[2] | Chenguang Zhang[1] | Teddy Salim[1] | Natalia Yantara[3] | Shixuan Du[2] | Nripan Mathews[1,3] | Kedar Hippalgaonkar[1,4]

[1]School of Materials Science and Engineering, Nanyang Technological University, Singapore, Singapore | [2]Institute of Physics and University of Chinese Academy of Sciences, Chinese Academy of Sciences, Beijing, China | [3]Energy Research Institute @ NTU (ERI@N), Nanyang Technological University, Singapore, Singapore | [4]Institute of Materials Research and Engineering (IMRE), Agency for Science, Technology and Research (A*STAR), Singapore, Singapore

Correspondence: Shixuan Du (sxdu@iphy.ac.cn) | Nripan Mathews (nripan@ntu.edu.sg) | Kedar Hippalgaonkar (kedar@ntu.edu.sg)

Received: 10 May 2026 | **Revised:** 24 July 2026 | **Accepted:** 31 July 2026

Keywords: alkali-cation doping | diffusion barrier | grain boundaries | ion migration

ABSTRACT

Lead halide perovskites exhibit outstanding optoelectronic properties, yet ion migration can influence device performance—detrimental in photovoltaics but beneficial in resistive-switching devices. Intrinsic ion migration has been extensively studied, whereas the effects of extrinsic alkali cations on field-driven ionic behavior remain less understood, particularly in lateral device architectures. Here, the effects of Li^+, Na^+, and K^+ incorporation on the ionic behavior of $MAPbBr_3$ thin films are investigated. Nanoscale and macroscopic measurements reveal cation-dependent ionic responses, which are particularly pronounced at grain boundaries and surfaces. Among the three cations, 1% Li^+ incorporation shows the strongest effect, yielding higher current and more pronounced hysteresis in lateral ITO/$MAPbBr_3$/ITO devices. The hysteresis index (H_{index}) increases from ~0.61 in the first cycle (−0.15 for the control) to ~0.85 after 20 cycles (~0.30 for the control), accompanied by ~40× higher current under identical conditions. Density functional theory (DFT) calculations further show cation-dependent differences in the calculated diffusion barriers at the (100) surface and across the N–N interfacial model, with Li^+ exhibiting the lowest barriers. These results indicate that extrinsic alkali-cation incorporation provides an effective approach to modulate ionic transport and hysteresis in lateral perovskite devices, offering insights for perovskite electronics where ionic effects play a key role.

1 | Introduction

Organic–inorganic lead halide perovskites (OLHPs) have garnered significant attention due to their exceptional optoelectronic properties, enabling widespread applications in photovoltaics and emerging electronic devices such as resistive-switching memories [1–4]. OLHPs typically adopt the ABX_3 structure, where A represents a monovalent organic or inorganic cation (e.g., MA^+, FA^+, Cs^+), B is a divalent metal cation (e.g., Pb^{2+} or Sn^{2+}), and X is a halide anion (e.g., Br^-, I^-, or Cl^-) [5]. Due to the weak interactions between the A cations and the BX_6 octahedra, the corner-sharing octahedral framework, and the antibonding interactions between Pb $6s^2$ and I $5p^6$ orbitals, OLHPs display a soft crystal lattice and mixed electronic–ionic behavior [6], which leads to ion migration under external factors such as electric fields, temperature, or illumination [7–11]. Recent experiments and first-principles simulations have shown that halide ions (I^-/Br^-) and their associated vacancies migrate more readily in OLHP films than other species, such as Pb^{2+} or $CH_3NH_3^+$, due to their lower activation and formation energies [12].

Ion migration in halide perovskite devices is a double-edged sword: detrimental in perovskite solar cells (PSCs), where it contributes to current–voltage (I-V) hysteresis and long-term instability, but beneficial in resistive-switching memory devices, enabling dynamic modulation of resistance states [13–15]. Li et al. [16] reported that extrinsic ions, such as Li^+ and Na^+, can originate from the hole transport layer (HTL) and migrate within PSCs, thereby potentially enhancing hysteresis and affecting device stability. These findings suggest that extrinsic ion migration, like intrinsic ion movement, can influence device performance and hysteresis behavior of perovskite-based devices. While most studies on alkali metal ions in PSCs have focused on device stability, their spatial distribution within OLHPs remains not fully understood due to variations in composition and processing. Reported incorporation sites include the A-site of the perovskite lattice [17, 18], interstitial positions [19, 20], and regions near surfaces and grain boundaries (GBs) [21–24], implying diverse migration pathways. Intrinsic ion transport in the bulk is typically governed by vacancy-mediated diffusion [12, 25], whereas GBs, with their higher defect densities, promote enhanced migration along GBs [26–28]. Most existing studies on alkali metal ions have focused on conventional vertical architectures [20, 29–32], typically in PSCs. Lateral electrode configurations have also been employed to probe ion migration, even in studies primarily focused on vertical devices [33–35]. Moreover, perovskite materials have also been explored in lateral device architectures for electronic applications, including photodetectors [36, 37], field-effect transistors [38, 39], and memristive devices [40, 41]. Understanding the behavior of extrinsic alkali ions in such lateral configurations is important for interpreting ionic effects in perovskite electronic devices.

Lateral perovskite devices, consisting of a symmetric electrode/halide perovskite/electrode structure (e.g., Au or ITO) [42], provide a convenient platform for investigating ion migration processes under an in-plane electric field. While gold (Au) electrodes are commonly used [43, 44], they can undergo interfacial reactions with halide perovskites, forming gold halides that introduce defects and degrade device performance [45–47]. To avoid these issues, interdigitated ITO electrodes are employed in this work, offering improved stability and uniformity for reliable evaluation of ion-migration-related hysteresis. Single-halide perovskites are selected to prevent phase segregation and halide redistribution [48], and multi-cation formulations (e.g., MA/FA/Cs) that may introduce lattice strain are avoided [49]. Accordingly, $MAPbBr_3$, with high phase purity and structural stability, is chosen as a suitable model system for alkali-ion addition studies [26, 27].

Despite extensive studies on extrinsic alkali cations in PSCs, ion migration has mainly been addressed as a stability issue to be mitigated in photovoltaic devices. Consequently, the potential role of extrinsic alkali ions in regulating field-driven ionic behavior in lateral perovskite devices remains insufficiently understood. Moreover, systematic comparisons of different alkali cations and their distinct effects on hysteresis in lateral device geometries are still limited. In this work, Li^+, Na^+, and K^+ are introduced into $MAPbBr_3$ thin films by adding alkali bromide salts to the precursor solutions to investigate how extrinsic alkali cations influence field-driven ion migration processes in lateral perovskite films. Lateral perovskite devices with interdigitated ITO electrodes are fabricated to quantify I–V hysteresis in this geometry. Film characterization and electrical measurements are combined to examine how alkali-cation incorporation affects film microstructure, current response, and hysteresis behavior, with a focus on ionic processes occurring near surfaces and grain boundaries. Among the three alkali cations, Li^+ produces the most pronounced changes in current response and hysteresis. DFT calculations further provide insight into the experimentally observed trend by comparing the diffusion barriers of Li^+, Na^+, and K^+ at representative perovskite interfaces. These results indicate that extrinsic alkali-cation incorporation provides an effective approach to tuning ionic dynamics and hysteresis in lateral halide perovskite devices.

2 | Results and Discussion

ITO-coated glass substrates (Figure 1a) are first patterned into interdigitated electrodes (Figure 1b), followed by spin coating of $MAPbBr_3$ precursor solutions containing 0% (control) or 1 mol% KBr, NaBr, or LiBr to form perovskite films (Figure 1c). The resulting lateral ITO/perovskite/ITO device structure used for electrical measurements is shown in Figure 1d. Figure 1e illustrates the ionic distribution scenarios near grain boundaries (GBs) considered in pristine and alkali-ion-modified perovskites. The ion migration behavior is experimentally evaluated through forward and reverse voltage sweeps to obtain the I–V characteristics (Figure 1f). Figure 1g summarizes the DFT-calculated diffusion barriers of K^+, Na^+, and Li^+ ions migrating along the (100) surface and across the N–N interface.

First, the possibility that the introduced alkali ions (K^+, Na^+, and Li^+) incorporate into the $MAPbBr_3$ lattice at the A-site or B-site is evaluated [50]. X-ray diffraction (XRD) analysis is performed to assess structural changes upon alkali-ion addition. The pronounced (100) diffraction peak suggests a preferred crystallographic orientation of the $MAPbBr_3$ films, which has also been reported in solution-processed $MAPbBr_3$ thin films with similar film structures [32, 51, 52]. The Li^+-doped film shows a stronger (100) reflection at ~15°, characteristic of the cubic phase (Figure 2a), whereas the Na^+- and K^+-doped films exhibit reduced peak intensities. Moreover, no detectable shift in the (100) peak position is observed for either 1% or 5% additive loading (Figure S1), indicating that any lattice substitution is below the detection limit of XRD. This trend is consistent with prior reports showing negligible lattice distortion upon alkali-cation doping [21]. At higher additive levels, additional reflections emerge in the XRD patterns, implying reduced phase purity; therefore, a 1% additive loading is chosen for subsequent analyses to ensure phase purity and isolate the influence of alkali ions on ion migration.

This inference is further supported by Goldschmidt's tolerance factor (t), where stable perovskite structures typically satisfy $0.8 < t < 1.0$. The ionic radii of K^+ (138 pm), Na^+ (102 pm), and Li^+ (76 pm) are significantly smaller than those of conventional A-site cations, such as MA^+ (217 pm) and FA^+ (253 pm). Consequently, the calculated t values for $MAPbBr_3$ assuming full A-site substitution by K^+, Na^+, or Li^+ fall within 0.61–0.75 (Figure S2a), which is below the typical stability range and therefore suggests that A-site incorporation is geometrically unfavorable. Solid-state ^{207}Pb NMR, which is sensitive to the local Pb–halide coordination environment [53, 54], is performed on $MAPbBr_3$ single

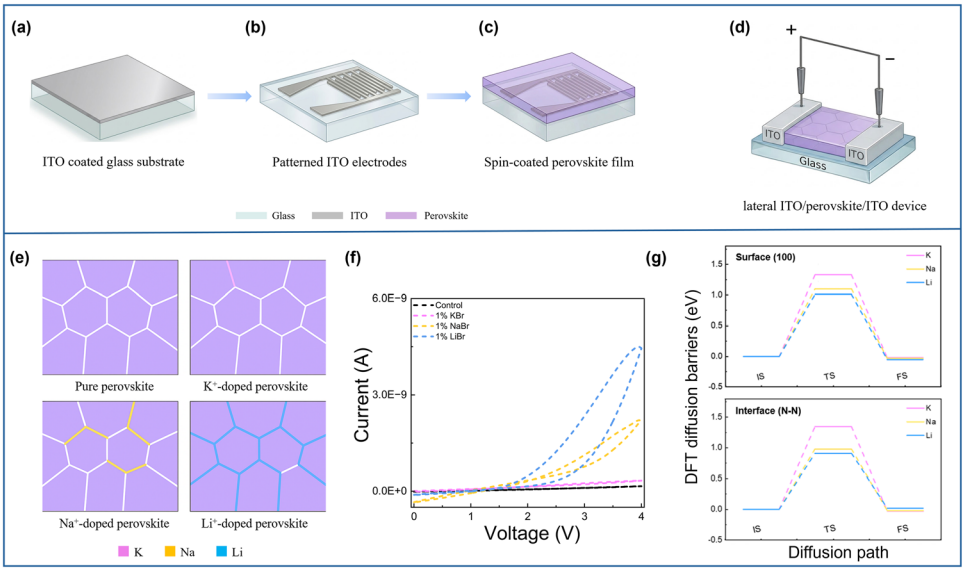

FIGURE 1 | Fabrication and ion-dependent transport in alkali-ion-modified $MAPbBr_3$ lateral devices. (a) ITO-coated glass substrate. (b) Patterned interdigitated ITO electrodes (electrode gap ≈ 200 μm). (c) Spin-coated perovskite thin film with or without alkali metal bromide additives (LiBr, NaBr, or KBr). The films were prepared via a one-step spin-coating process followed by thermal annealing. (d) Schematic illustration of the lateral ITO/perovskite/ITO device used for electrical measurements. (e) Schematic illustration of ion distributions near grain boundaries (GBs) for pristine and M^+ (Li^+/Na^+/K^+)-modified perovskites. (f) I–V characteristics measured under forward and reverse voltage sweeps, revealing doping-dependent hysteresis behavior associated with ion migration in the perovskite films. (g) DFT-calculated diffusion barriers of K^+, Na^+, and Li^+ ions migrating along the (100) surface and across the N–N interface, used to compare cation-dependent diffusion characteristics at representative perovskite interfaces.

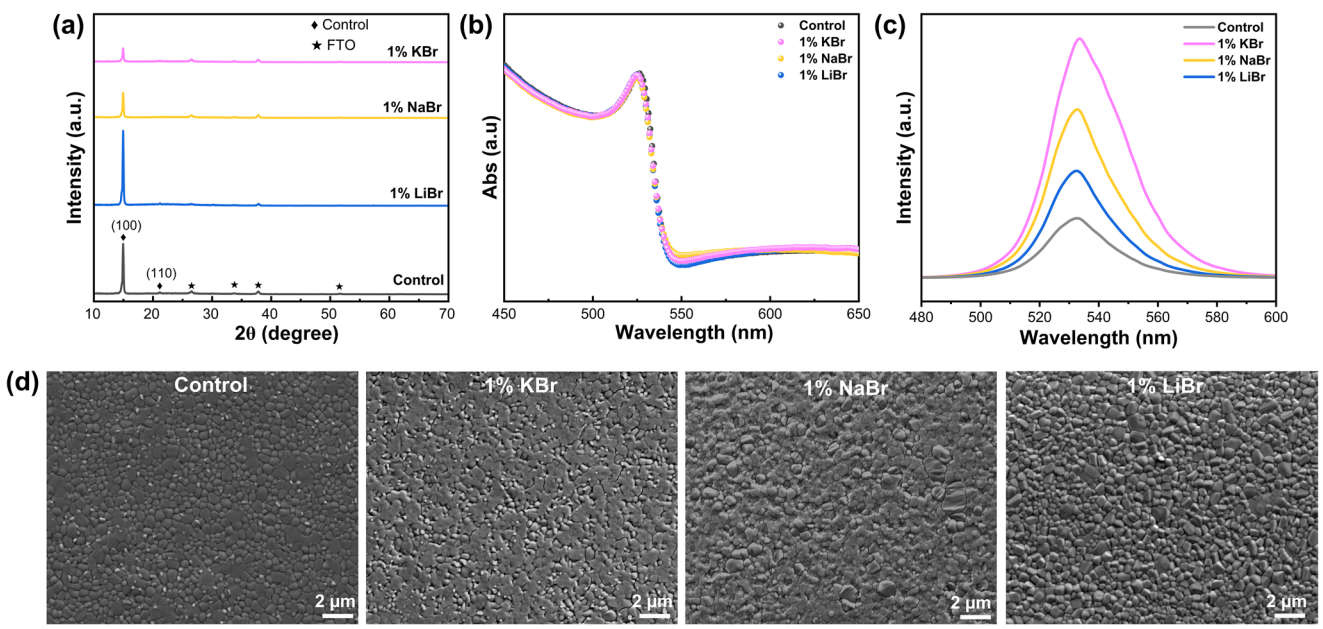

FIGURE 2 | (a) XRD patterns of $MAPbBr_3$ (Control) and films with 1% KBr, NaBr, or LiBr addition; (b) UV–vis absorbance spectra of the same samples; (c) PL spectra of the same samples. (d) Top-view SEM images of the control and films with 1% KBr, NaBr, or LiBr addition (left-to-right). Scale bars: 2 μm.

crystals grown with 20 mol% additives to enhance detectability (Figure S2b). The negligible change in ^{207}Pb chemical shifts suggests that the Pb–Br coordination remains largely intact, indicating no significant perturbation of the B-site environment. Overall, these results indicate that bulk lattice incorporation of K^+, Na^+, and Li^+ is limited.

The UV-vis absorption spectra (Figure 2b) exhibit a characteristic absorption edge at ~540 nm, typical of bromide-based perovskites. Tauc plot analysis (Figure S3) reveals no noticeable change in the optical bandgap, which remains around 2.29 eV for the control and the films with 1% and 5% alkali-ion addition. These results indicate that introducing K^+, Na^+, or Li^+

at these loadings does not significantly alter the absorption edge or bandgap of $MAPbBr_3$. Steady-state photoluminescence (PL) spectra (Figure 2c) show similar peak positions for all samples, indicating that the bandgap of $MAPbBr_3$ is not altered by alkali-ion incorporation. Minor variations in PL intensity are observed among the films, which may be related to differences in recombination behavior [31, 32]. Surface-sensitive X-ray photoelectron spectroscopy (XPS) further verifies the presence of monovalent alkali ions in the perovskite films (Figure S4). Distinct signals corresponding to the Li 1s, Na 1s, and K 2p peaks are detected, indicating that these cations are present at the film surface or near-surface region [31, 55]. The planar-view SEM images (Figure 2d) reveal that alkali-ion addition influences the surface morphology of $MAPbBr_3$ films. Although the differences are subtle in the top-view images, the film with Li^+ addition tends to exhibit larger and more compact grains with fewer visible pinholes, whereas the Na^+- and K^+-treated films exhibit relatively smaller and less uniform grains. Cross-sectional SEM images (Figure S5) further show that 1% Li^+ addition results in enlarged grains and clearly discernible GBs. In contrast, the Na^+-treated films display irregular grain sizes and less uniform grain alignment, whereas the K^+-treated film closely resembles the pristine $MAPbBr_3$ film, suggesting that this additive has only a relatively minor influence on film growth and GB formation. AFM analysis (Figure S6) further shows a gradual increase in surface roughness from 7.47 nm for the control film to 14.3 nm for the film with Li^+ addition. These structural and morphological characterizations support that the added alkali ions do not incorporate into the $MAPbBr_3$ lattice but instead induce measurable modifications at the surface and GB regions. To evaluate how these microstructural changes influence local charge transport behavior, conductive atomic force microscopy (c-AFM) is employed.

The c-AFM current maps provide nanoscale spatial information on local conduction pathways across the perovskite films. Figure 3 shows the aligned topography and corresponding current maps of $MAPbBr_3$ films with alkali-ion addition, processed from the raw data in Figure S7 to enable direct spatial comparison among different samples. The pristine $MAPbBr_3$ film (Figure 3a) exhibits a largely uniform current distribution with little contrast between grain interiors and GBs, indicating relatively homogeneous local conduction in the absence of alkali-ion addition. A similar behavior is observed for the 1% K^+-doped film (Figure 3b), suggesting that K^+ has a minimal influence on the local current distribution. In contrast, the 1% Na^+-doped sample (Figure 3c) displays localized current enhancement at certain GBs, but the pronounced variations across different GBs indicate spatially discontinuous conduction pathways. Notably, the 1% Li^+-doped film (Figure 3d) exhibits the most pronounced current contrast between GBs and grain interiors, with enhanced and more spatially continuous current features associated with GB regions. These spatial features suggest that alkali-ion addition, particularly Li^+, is associated with modifications in the spatial distribution of local current in the perovskite films, with GB regions exhibiting enhanced local current relative to grain interiors. To further quantify the spatial variations observed in the c-AFM current maps, line-scan current profiles are extracted along the representative traces indicated in Figure 3 and Figures S8–S11. The pristine and 1% K^+-doped films exhibit nearly identical current profiles across grains and GBs, consistent with their largely uniform current maps. In the 1% Na^+-doped film, the two profiles deviate noticeably at several GB locations, reflecting pronounced spatial variations in current along different GBs. By contrast, the 1% Li^+-doped film shows highly similar current values at corresponding positions along the two line scans, indicating a more consistently enhanced local current response near GB regions.

To correlate the nanoscale conduction behavior with macroscopic transport behavior, DC galvanostatic polarization measurements are performed under dark conditions using the same interdigitated ITO electrodes, allowing the electronic (σ_e) and ionic (σ_{ionic}) conductivities to be distinguished (Figure 3e,f). In this measurement, the initial voltage jump reflects total conductivity σ_{total} ($\sigma_{total} = \sigma_{ionic} + \sigma_e$, Figure S12), whereas the steady-state voltage corresponds to σ_e, and σ_{ionic} is subsequently obtained from the difference between σ_{total} and σ_e [56]. All films exhibit mixed ionic–electronic conduction characteristics. The σ_e of the 1% K^+-doped film is nearly identical to that of pristine $MAPbBr_3$, whereas the Na^+- and Li^+-doped films show a slight increase in σ_e, which may arise from subtle surface or interfacial electronic effects in addition to the intrinsically p-type nature of $MAPbBr_3$ [57]. For σ_{ionic}, both Na^+- and Li^+-doped samples display an order of magnitude enhancement relative to the control and K^+-doped films. This pronounced enhancement in σ_{ionic} is consistent with the enhanced local current observed by c-AFM, suggesting that Na^+ and particularly Li^+ exhibit enhanced local conduction, whereas K^+ exerts a comparatively limited influence. Overall, these results indicate that alkali-ion incorporation mainly influences ionic transport behavior in the films, with Li^+-doped films exhibiting the most substantial effect. Building on these findings, the field-driven ionic response is further investigated through nanoscale c-AFM I–V measurements and device-level I–V measurements using lateral ITO/$MAPbBr_3$/ITO devices.

Bias-sweep I–V hysteresis is used below as a comparative indicator of field-driven ion migration, measured on lateral devices with interdigitated ITO electrodes (Figure 1b). The I–V hysteresis increases with temperature (Figure S13), consistent with thermally activated ionic dynamics. At low temperatures, ionic movement is suppressed, whereas higher temperatures provide sufficient thermal energy to facilitate ion migration under bias. This temperature-dependent behavior suggests that the hysteresis is closely associated with ion migration, as reported in previous studies identifying ion migration as a key contributor to hysteresis in perovskite devices [58–60]. While ferroelectricity [61] and charge trapping [62] have been proposed as alternative origins of hysteresis, the characteristic timescales of these processes are much shorter than those of the slow-scan hysteresis typically observed [63, 64], suggesting that ion migration likely plays a major role under the present measurement conditions. To evaluate how ionic effects vary with the alkali cation, local c-AFM I–V measurements are performed at multiple GB locations for four films. The 1% Li^+-doped film (Figure 4b) exhibits a pronounced counter-clockwise hysteresis loop, whereas the undoped $MAPbBr_3$ film (Figure 4a) shows a small clockwise loop (see Figure S14 for measurement positions). Such a reversal in loop direction and enlargement of the hysteresis window are consistent with enhanced field-driven ionic responses at GBs, pointing to more active ionic behavior in the Li^+-doped film under bias. In contrast, the Na^+-doped film (Figure S15c,d) shows a moderate increase in hysteresis relative to the control,

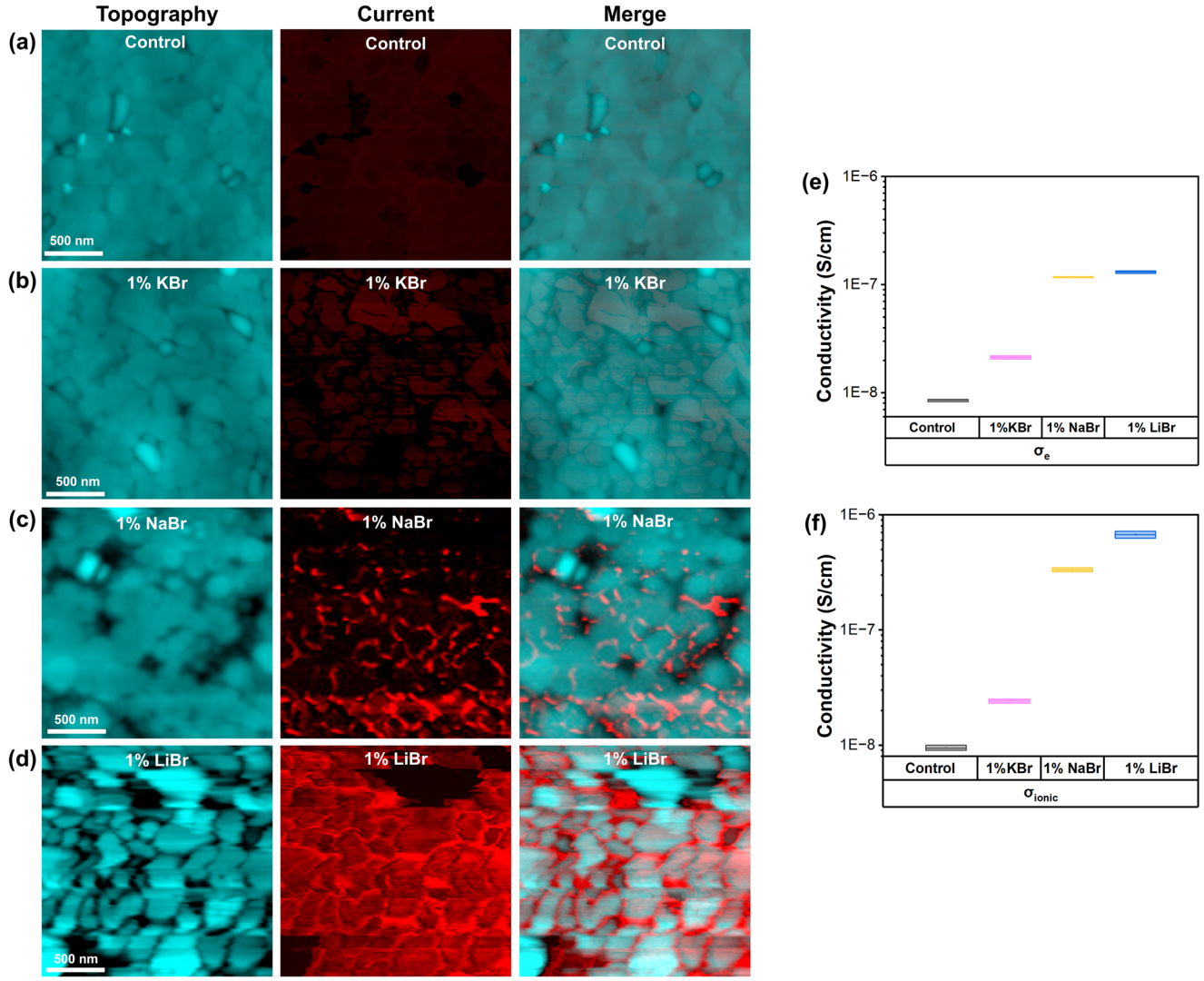

FIGURE 3 | Dopant-dependent local conduction in $MAPbBr_3$ films revealed by c-AFM and DC polarization. (a–d) Topography, current, and merged c-AFM maps of (a) Control, (b) 1 mol% KBr, (c) 1 mol% NaBr, and (d) 1 mol% LiBr films, measured in the dark under ambient atmosphere at a bias of 0.5 V. (e) Electronic conductivity (σ_e) and (f) ionic conductivity (σ_{ionic}) extracted from DC galvanostatic polarization measurements for the corresponding films, following the trend σ_{ionic} (Li^+) > σ_{ionic} (Na^+) > σ_{ionic} (K^+) ≈ σ_{ionic} (Control), consistent with the c-AFM current contrast.

whereas the K^+-doped film (Figure S15a,b) displays nearly identical hysteresis behavior to the control, implying that K^+ has a comparatively limited influence on ion migration behavior. The c-AFM I–V trends are consistent with the current-mapping results and suggest a more pronounced GB-associated ionic contribution to local conduction in the Li^+ films, with a weaker but similar effect for Na^+. Previous studies have shown that ion migration in OLHPs often occurs preferentially at GBs, where stronger hysteresis is typically observed than within grain interiors [27]. Since GBs are widely reported to act as preferential pathways for ion migration in polycrystalline perovskite films, the similar ionic trends observed locally at GBs may contribute to the device-level I–V characteristics.

The I–V characteristics of lateral $MAPbBr_3$ devices are measured under repeated bias sweeps. Figure 4c,d present the cyclic I–V curves of the control and Li^+-doped $MAPbBr_3$ devices measured at 4 V with a scan rate of 0.05 V s^{-1}. These conditions are selected to ensure that all samples exhibit measurable hysteresis under dark conditions, enabling reliable comparison of field-driven ionic effects. The choice is supported by systematic variations in bias (2-4 V) and scan rate (0.5–0.05 V s^{-1}) (Figures S16–S19), which show that the Li^+-doped devices display the most pronounced hysteresis across the tested conditions. The device-level hysteresis in the Li^+-doped samples (Figure 4c,d) follows the same cation-dependent trend as the nanoscale c-AFM I–V hysteresis, with the Li^+-containing film exhibiting the most pronounced response, followed by the Na^+-containing film, while the K^+-containing film remains similar to the control. Under these conditions, all devices display reproducible hysteresis loops over 20 consecutive cycles with minimal changes in loop shape, indicating stable field-driven ionic behavior. The control device (Figure 4c) shows a relatively narrow hysteresis window and weak current response, whereas the Li^+-doped device (Figure 4d) exhibits higher current levels and a broader loop, indicating more pronounced field-driven ionic dynamics. The Na^+- and K^+-doped devices (Figure S20) show similar cyclic trends, while the extent of hysteresis varies significantly: the K^+-doped devices behave almost

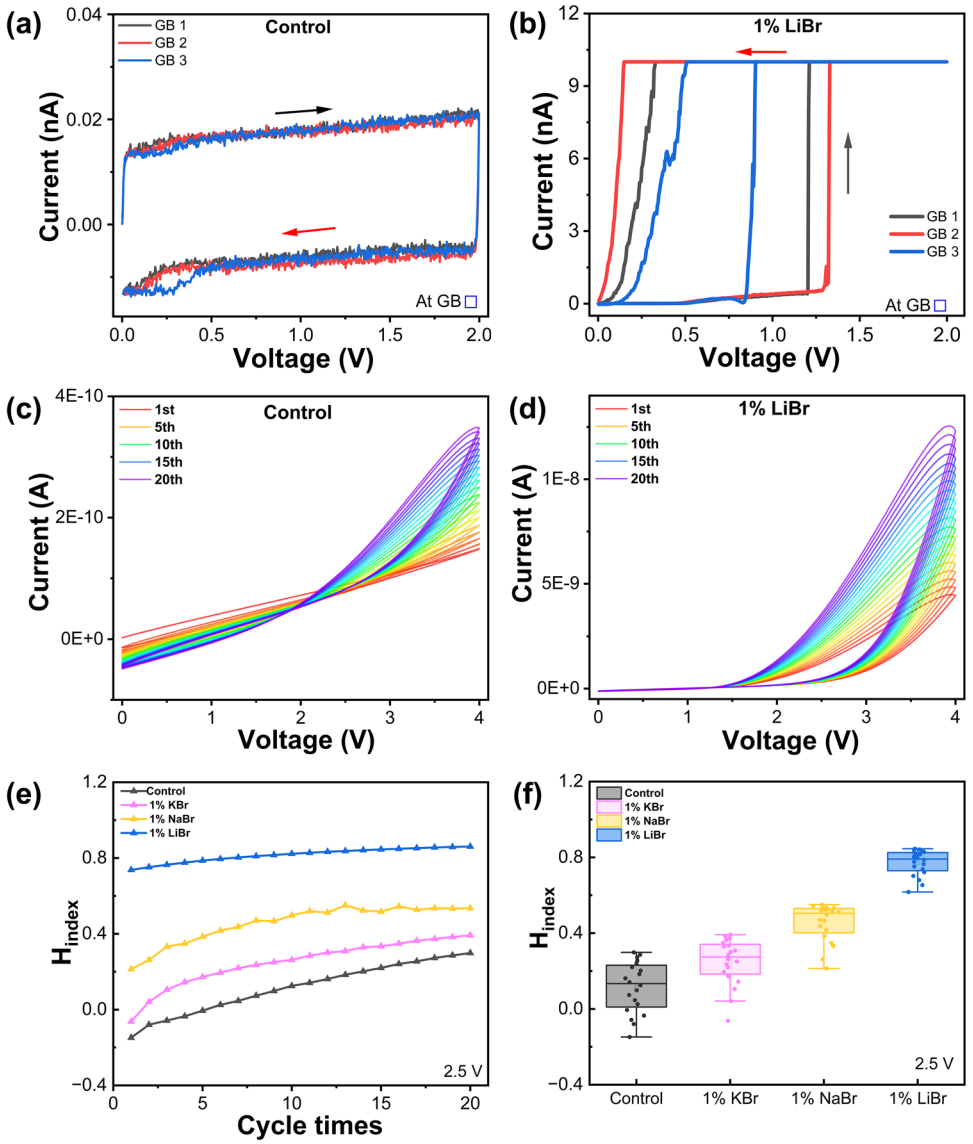

FIGURE 4 | Hysteresis behavior in metal-ion-doped $MAPbBr_3$ samples. (a,b) Local I–V characteristics measured by c-AFM in the dark at three GB locations (black, red, and blue squares) for the control and 1% Li^+-doped $MAPbBr_3$ films. (c,d) Cyclic I–V curves of lateral devices for the control and 1% Li^+-doped samples measured over 20 consecutive cycles at 4 V with a scan rate of 0.05 V s^{-1}. (e,f) Quantitative comparison of the hysteresis index (H_{index}) extracted at 2.5 V from cyclic I–V measurements.

identically to the control, suggesting a minor effect on ionic dynamics, whereas the Na^+-doped devices exhibit an intermediate response between K^+ and Li^+. These results support that the cyclic hysteresis is closely associated with field-driven ionic motion and varies systematically with the alkali-cation incorporation. Although vertical c-AFM evaluates localized transport through the sub-micrometer film thickness and primarily probes surface-dominated GB regions, lateral devices evaluate collective in-plane transport across a 200 μm channel involving both the film bulk and buried substrate interfaces. However, the local c-AFM measurements and the lateral devices exhibit a similar cation-dependent trend. Together with the columnar grain structure of the films, where the GBs extend continuously through the film thickness, the c-AFM results provide spatially resolved evidence supporting the cation-dependent trends observed in the lateral devices.

To quantitatively evaluate the hysteresis behavior, the hysteresis index (H_{index}) is extracted from cyclic I–V measurements performed under a 4 V sweep, using current values at a bias point of 2.5 V (Figure 4e,f). Defined as $(I_{reverse}—I_{forward})/I_{reverse}$ (Figure S21), H_{index} quantifies the extent of hysteresis and serves as a comparative metric of ionic effects related to ion migration. Higher H_{index} values are generally correlated with stronger ionic effects, whereas lower (or negative) values indicate suppressed ion migration. All samples show a gradual increase in H_{index} over 20 cycles, indicating reproducible field-driven ionic responses. The Li^+-doped device exhibits the highest and most stable H_{index} values (0.62 to 0.85), consistent with more pronounced and persistent ionic behavior. The Na^+-doped sample shows a moderate increase (0.21 to 0.54), whereas the K^+-doped and control devices remain nearly comparable (–0.15 to 0.30 and –0.06 to 0.39, respectively). The consistent hierarchy of H_{index} (Li^+

> Na^+ > K^+ ≈ control) suggests that Li^+ doping corresponds to the most pronounced enhancement of device-level ionic hysteresis in $MAPbBr_3$. To further verify the cycling stability, the 1% Li^+-doped device is subjected to extended measurements over 200 consecutive cycles. As shown in Figure S22, the hysteresis behavior remains well maintained throughout the prolonged cycling test.

XPS analysis (Figure S23) is performed to examine the chemical environment of the metal-ion-doped $MAPbBr_3$ films. The Br/Pb ratios for the K^+-, Na^+-, and Li^+-doped samples are 2.78, 2.85, and 2.95, respectively, slightly higher than that of the undoped reference (2.72). This modest increase in Br/Pb ratio indicates that incorporating metal bromide salts leads to a slightly Br-rich environment during film formation [65]. However, the relatively small variation in composition suggests that it may not be the dominant factor governing the observed differences in ionic behavior. To further understand the role of alkali cations in influencing ionic transport, first-principles calculations based on density functional theory (DFT) are performed to evaluate the diffusion pathways and migration energy barriers of different alkali ions. For this purpose, the surface termination and GB interface of $MAPbBr_3$ are first established to construct representative structural models for diffusion analysis.

To investigate ion migration at grain boundaries, we first identify the stable surface termination of $MAPbBr_3$. Five surface configurations are constructed for the (100), (010), and (001) facets, each with different orientations of the $CH_3NH_3^+$ (MA^+) molecules (Figure S24). Among them, the (100) surface, with the NH_3 group of $CH_3NH_3^+$ oriented toward the surface (inset of Figure 5a), exhibits the lowest energy, indicating that it is the most stable configuration. This theoretical result is consistent with the predominant (100) orientation observed in the XRD measurements (Figure 2a), supporting the relevance of this configuration to the experimental system. Grain boundaries in polycrystalline perovskites are interfaces formed between adjacent grains. Given that low-index planes generally possess the lowest surface energies and are preferentially exposed during crystal growth, grain boundaries are predominantly composed of interfaces between such stable facets. Therefore, we construct an N-N interface grain-boundary model using two (100) surfaces with the NH_3 groups of adjacent $CH_3NH_3^+$ molecules facing each other (zoom-in view in Figure 5b). The interface distance is 3.94 Å (Figure 5b, right; Figure S25), which serves as the basis for subsequent diffusion calculations. Next, the adsorption sites for K, Na, and Li species are systematically explored on the (100) surface. As shown in Figure S26, twelve potential adsorption sites are initially considered for each species. After relaxation, three adsorption sites are identified, namely the hole, Pb-top, and Br-bridge sites (Figure 5c). K and Na preferentially adsorb at the hole or Pb-top sites, whereas Li also shows the ability to bind at the Br-bridge site. By comparing the total energies of K, Na, and Li adsorbed on the (100) surface, the hole site is found to be the most stable for all three atoms. Therefore, the adsorption configurations with K, Na, and Li at the hole site are adopted as both the initial and final states in subsequent investigations of surface diffusion processes. The interface diffusion analysis likewise employs the adsorption configurations at the hole site, as depicted in Figure S27.

Using these configurations, the diffusion behavior of K, Na, and Li on the surface and at the interface of $MAPbBr_3$ is analyzed. Although the N–N interface structure is adopted in the main simulations, additional interface models are evaluated to ensure the structural reliability. Specifically, two alternative configurations are tested: one with CH_3 groups facing each other (C–C) and another with CH_3 facing NH_3 (C–N). The C–C configuration is excluded because the molecules rotated toward the N–N alignment during relaxation (Figure S29), while the C–N configuration is ruled out due to significant lattice distortion caused by ion adsorption (Figure S30). On the (100) surface, the calculated diffusion barriers follow the order K (1.33 eV) > Na (1.10 eV) > Li (1.01 eV), indicating that Li diffuses the fastest and K the slowest (Figure 5e). A similar trend is observed at the interface, where the barriers are K (1.35 eV) > Na (0.98 eV) > Li (0.91 eV) (Figure 5f). Thus, among the examined cations, Li exhibits the lowest diffusion barriers on the (100) surface and at the N–N interface.

Based on the XPS, PL, SEM, DC galvanostatic polarization, c-AFM, and DFT results, we attribute the enhanced hysteresis primarily to alkali-salt-induced modification of the perovskite film, which includes alkali-salts-induced surface morphology modification while possible direct migration of the incorporated alkali cations may provide an additional contribution. Alkali-salt incorporation modifies the film composition, surface morphology, and film quality, which may alter ion migration within the host perovskite. The increased XPS-derived Br/Pb ratio signifies reduced Br^- vacancies, whereas the enhanced absorbance-normalized PL intensity suggests reduced non-radiative recombination. However, neither observation alone explains the increased ionic transport. Adding alkali salts also increases surface roughness, which may create a more defect-rich surface region that promotes ion migration. In addition, the small alkali cations are also prone to ionic migration. The calculated diffusion-barrier hierarchy of Li^+ < Na^+ < K^+ further suggests that the incorporated alkali cations may contribute to ionic migration, although the mobile ionic species cannot be directly identified. Because alkali-induced film modification and possible direct alkali-ion migration may contribute simultaneously, their relative contributions cannot be quantitatively separated based on the present measurements.

3 | Conclusion

This study indicates that alkali-cation incorporation can modulate the field-driven ionic behavior in $MAPbBr_3$ thin films. LiBr-, NaBr-, and KBr-treated lateral devices exhibit distinct hysteresis characteristics, with the effective ionic response following the order LiBr > NaBr > KBr ≈ control and the LiBr-treated devices exhibiting the largest hysteresis and current response. Based on the combined experimental and computational results, we attribute the enhanced hysteresis primarily to alkali-salt-induced modification of the perovskite film, while possible direct migration of the incorporated alkali cations may provide an additional contribution. Although the mobile ionic species cannot be directly identified and the relative contributions of these processes cannot be quantitatively separated, the results establish a clear cation-dependent influence on the ionic response of $MAPbBr_3$. These findings provide insight into how different

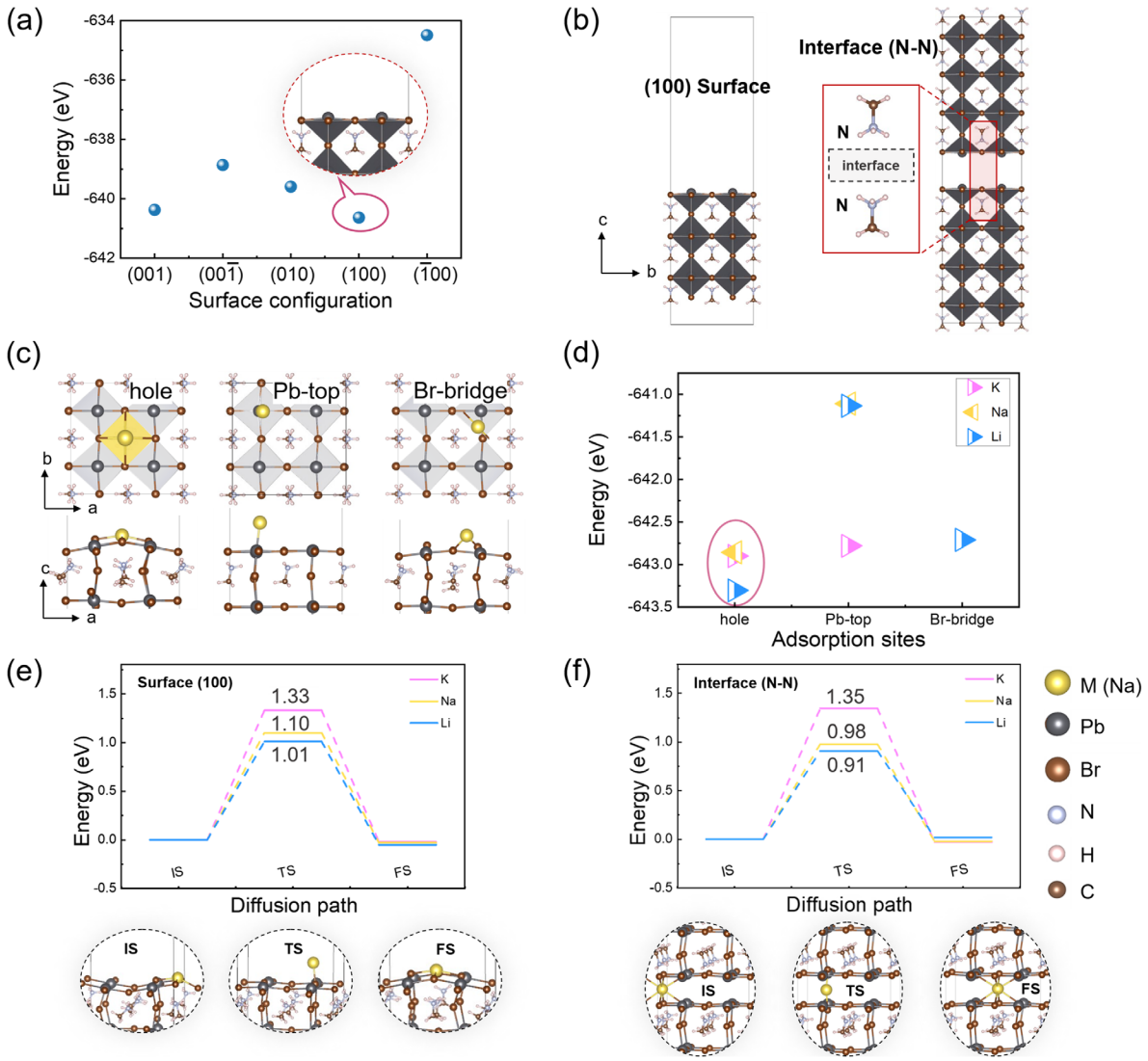

FIGURE 5 | Surface and interface configurations of $MAPbBr_3$ and adsorption sites for K, Na, and Li. (a) Energy comparison of five surface configurations, highlighting that the (100) surface with the NH_3 group of CH_3NH_3 close to the surface has the lowest energy (see insert). (b) Side views of the (100) surface and the interface. The zoom-in figure exhibits that the NH_3 groups face each other at the interface. (c) Configurations for three screened-out adsorption sites: hole, Pb-top, and Br-bridge. (d) Total energies of K, Na, Li adsorption on (100) surface, identifying the hole position as the most stable adsorption site for all the three atoms. (e) Energy barriers for the diffusion of K, Na, Li between adjacent hole sites on the (100) surface. The bottom panels are the configurations of the initial, transition, and final states of Na on the surface during the diffusion process. (f) Energy barriers for the diffusion of K, Na, and Li between adjacent hole sites at the interface. The bottom panels are the configurations of the initial, transition, and final states of Na at the interface during the diffusion process. The configurations for K and Li diffusing at the surface/interface are summarized in Figure S28.

extrinsic cations influence ion migration behavior in halide perovskites and highlight cation engineering as a potential strategy for tuning ion-related behavior in perovskite electronic and memristive devices.

4 | Experimental Section

4.1 | Chemicals and Materials

Methylammonium bromide (MABr) was purchased from Greatcell Solar, and lead bromide ($PbBr_2$) was sourced from Tokyo Chemical Industry. Lithium bromide (LiBr), sodium bromide (NaBr), and potassium bromide (KBr), used as metal ion sources, were obtained from Sigma-Aldrich. Additionally, the solvents N,N-dimethylformamide (DMF), dimethyl sulfoxide (DMSO), and the antisolvent toluene were also procured from Sigma-Aldrich.

4.2 | ITO Substrate Preparation

For sputtered interdigital ITO (90:10 wt% In_2O_3:SnO_2), electrodes with a 200 μm gap were deposited via magnetron sputtering using a 50 W (~2.5 W/cm^2) DC power source at a chamber pressure of 5 mTorr. The company-customized interdigital ITO electrodes were

fabricated with the same 200 μm electrode gap. Prior to use, the 2.5 × 2.5 cm ITO substrates were sequentially cleaned by sonication for 15 min each in decon soap, deionized (DI) water, acetone, and isopropyl alcohol (IPA) to ensure a contaminant-free surface.

4.3 | Perovskite Precursor Solution and Lateral Device Fabrication

The precursor solutions were first prepared by dissolving 1 M MABr, 1 M $PbBr_2$, and 0.01 M of alkali metal bromide salts—specifically LiBr, NaBr, and KBr—in a mixed solvent of N,N-dimethylformamide (DMF) and dimethyl sulfoxide (DMSO) with a volume ratio of 5:2. The resulting solutions, each containing one type of alkali metal additive, were stirred at room temperature for at least 2 h to ensure complete dissolution and homogeneity. The precursor solutions were subsequently deposited onto pre-cleaned indium tin oxide (ITO)-coated glass substrates using a one-step spin-coating process. The spin-coating was performed at a speed of 6000 revolutions per minute (rpm) for 40 s. During the spin-coating process, 200 μL of toluene was swiftly dripped onto the rotating substrate at the seventh second to act as an antisolvent, promoting rapid crystallization of the perovskite film. Following deposition, the films were immediately transferred to a hotplate and annealed at 100 °C for 10 min in an ambient atmosphere to complete the crystallization of the $MAPbBr_3$-based perovskite layer. This process yielded uniform $MAPbBr_3$ films, including the undoped control and Li^+-, Na^+-, and K^+-doped samples. These films were employed as active layers in lateral perovskite memristor devices to investigate the effects of alkali metal ion doping on film morphology, crystallinity, and ion migration behavior.

4.4 | Characterizations

Scanning electron microscopy (SEM, JSM-7800F PRIME) was employed to observe the planar and cross-sectional morphologies of the samples. Atomic force microscopy (AFM, Park Systems NX10) was used to capture the surface topography of the films. The crystal phase of the perovskite films was analyzed using X-ray diffraction (XRD) with Cu Kα radiation (λ = 0.154 nm). Ultraviolet-visible-near infrared (UV–Vis–NIR) absorption spectra were recorded using a Shimadzu UV-2400 spectrophotometer. Photoluminescence spectroscopy (PL) spectra were obtained using a WITec alpha 300RAS confocal Raman microscope, with a linearly polarized continuous-wave (CW) solid-state laser at 405 nm serving as the excitation source. Elemental analysis was performed using X-ray photoelectron spectroscopy (XPS) on a Kratos AXIS Supra with aluminum X-ray monochromatic sources. Conductive atomic force microscopy (c-AFM) was performed with Cr/Pt-coated conductive tips (ElectriMulti75-G) having a 25 nm radius of curvature, enabling the simultaneous measurement of current and surface topography. All images were obtained with a bias voltage of 0.5 V under ambient conditions in the dark. The c-AFM measurements were conducted in a vertical configuration to map the nanoscale current distribution across the perovskite film surface. The resulting current maps provide spatially resolved information on the local current response at grain interiors and grain-boundary regions.

4.5 | Lateral Device Measurements

Galvanostatic direct current (d.c.) polarization measurements were carried out using a Keithley source meter integrated with a Lakeshore cryogenic probe station under a continuously pumped nitrogen atmosphere. For the DC polarization analysis, the ITO contacts were treated as nominally ion-blocking contacts. Under this approximation, the initial response contains contributions from both ionic and electronic charge carriers. During polarization, ionic redistribution progressively reduces the net ionic contribution, and the steady-state response is assigned to the electronic contribution, following the blocking-electrode polarization principle for mixed ionic–electronic conductors [66]. The effective ionic contribution was estimated from the difference between the initial total conductance and the steady-state conductance. The extracted ionic and electronic conductivities were used primarily to compare the relative transport trends among devices measured using the same electrode configuration and polarization. The initial total conductance and steady-state conductance were calculated as $G_0 = I/V_0$ and $G_{ss} = I/V_{ss}$, respectively. The effective ionic conductance was estimated as $G_{ion} = G_0 - G_{ss}$, while the electronic conductance was taken as $G_e = G_{ss}$. The corresponding conductivities were calculated using $\sigma = GL/A$, where L is the electrode spacing and A is the effective cross-sectional area of the perovskite channel [43].

Current–voltage (I–V) measurements were performed using the same vacuum probe station under continuous pumping, applying various bias voltages and scan rates to evaluate hysteresis behavior and ion migration characteristics. To quantify hysteresis, the hysteresis index (H_{index}) was calculated using the following equation: $H_{index} = (I_{reverse} — I_{forward})/ I_{reverse.}$ Within the same voltage range, a higher H_{index} value indicates more pronounced ion migration, while a lower value corresponds to suppressed ion migration.

4.6 | Calculation Method

Density functional theory (DFT) calculations are performed using the Vienna ab initio simulation package [67, 68], with the Perdew-Burke-Ernzerhof (PBE) functional within the generalized gradient approximation [69]. For surface configurations, the vacuum lengths are larger than 20 Å to avoid interaction between neighboring slabs. Dipole corrections are applied to account for the dipole-dipole interactions along the z-direction [70]. The bottom layer of the surface slab is fixed while the top two layers are fully relaxed. For the interface configurations, both the bottom and top two atomic layers are fixed, with the intermediate layers allowed to relax. For all the calculations, the electronic wave functions are expanded in plane waves with a kinetic energy cutoff of 450 eV, and the first Brillouin zone is sampled using a (2 × 2 × 1) T-centered k-mesh [71]. The convergence criteria for energy and force are set to 10–5 eV and 0.05 eV/Å, respectively. A dispersion correction of total energy (DFT-D3 method of Grimme with zero-damping function) is used to incorporate the van der Waals interaction [72, 73].

To investigate the diffusion mechanisms of K, Na, and Li atoms on the $MAPbBr_3$ surface/interface, the climbing image nudged

elastic band (CI-NEB) method [74, 75] is implemented using the Transition State Tools for VASP (VTST). Both the initial and final structures are fully relaxed until the residual force on each of the relaxed atoms was smaller than 0.05 eV/Å. Seven intermediate states are constructed by using linear interpolation, with the force convergence criterion set to 0.05 eV/Å.

Acknowledgements

This research was supported by the National Research Foundation (NRF), Singapore, under its Competitive Research Program (CRP) (NRF-CRP25-2020-0002) and NRF-NRFI10-2024-0002, and by the National Natural Science Foundation of China (Grant No. 62488201).

Conflicts of Interest

The authors declare no competing financial interest.

Data Availability Statement

The data that support the findings of this study are available from the corresponding author upon reasonable request.

References

1. H. Kim, J. S. Han, J. Choi, S. Y. Kim, and H. W. Jang, "Halide Perovskites for Applications Beyond Photovoltaics," *Small Methods* 2 (2018): 1700310, https://doi.org/10.1002/smtd.201700310.

2. X. Zhao, H. Xu, Z. Wang, Y. Lin, and Y. Liu, "Memristors With Organic-Inorganic Halide Perovskites," *InfoMat* 1 (2019): 183–210, https://doi.org/10.1002/inf2.12012.

3. J. Choi, J. S. Han, K. Hong, S. Y. Kim, and H. W. Jang, "Organic–Inorganic Hybrid Halide Perovskites for Memories, Transistors, and Artificial Synapses," *Advanced Materials* 30 (2018): 1704002, https://doi.org/10.1002/adma.201704002.

4. M. Vasilopoulou, A. R. bin Mohd Yusoff, Y. Chai, et al., "Neuromorphic Computing Based on Halide Perovskites," *Nature Electronics* 6 (2023): 949–962, https://doi.org/10.1038/s41928-023-01082-z.

5. Y. Fu, H. Zhu, J. Chen, M. P. Hautzinger, X.-Y. Zhu, and S. Jin, "Metal Halide Perovskite Nanostructures for Optoelectronic Applications and the Study of Physical Properties," *Nature Reviews Materials* 4 (2019): 169–188, https://doi.org/10.1038/s41578-019-0080-9.

6. E. Bi, Z. Song, C. Li, Z. Wu, and Y. Yan, "Mitigating ion Migration in Perovskite Solar Cells," *Trends in Chemistry* 3 (2021): 575–588, https://doi.org/10.1016/j.trechm.2021.04.004.

7. W. Zhu, S. Wang, X. Zhang, A. Wang, C. Wu, and F. Hao, "Ion Migration in Organic–Inorganic Hybrid Perovskite Solar Cells: Current Understanding and Perspectives," *Small* 18 (2022): 2105783.

8. S. Bae, S. Kim, S.-W. Lee, et al., "Electric-Field-Induced Degradation of Methylammonium Lead Iodide Perovskite Solar Cells," *The Journal of Physical Chemistry Letters* 7 (2016): 3091–3096, https://doi.org/10.1021/acs.jpclett.6b01176.

9. G. Divitini, S. Cacovich, F. Matteocci, L. Cinà, A. Di Carlo, and C. Ducati, "In Situ Observation of Heat-Induced Degradation of Perovskite Solar Cells," *Nature Energy* 1 (2016): 15012, https://doi.org/10.1038/nenergy.2015.12.

10. D. W. deQuilettes, W. Zhang, V. M. Burlakov, et al., "Photo-Induced Halide Redistribution in Organic–Inorganic Perovskite Films," *Nature Communications* 7 (2016): 11683, https://doi.org/10.1038/ncomms11683.

11. Y.-C. Zhao, W.-K. Zhou, X. Zhou, K.-H. Liu, D.-P. Yu, and Q. Zhao, "Quantification of Light-Enhanced Ionic Transport in Lead Iodide Perovskite Thin Films and its Solar Cell Applications," *Light: Science and Applications* 6 (2017): 16243.

12. C. Eames, J. M. Frost, P. R. F. Barnes, B. C. O'Regan, A. Walsh, and M. S. Islam, "Ionic Transport in Hybrid Lead Iodide Perovskite Solar Cells," *Nature Communications* 6 (2015): 7497, https://doi.org/10.1038/ncomms8497.

13. T. Zhang, C. Hu, and S. Yang, "Ion Migration: A "Double-Edged Sword" for Halide-Perovskite-Based Electronic Devices," *Small Methods* 4 (2020): 1900552, https://doi.org/10.1002/smtd.201900552.

14. K. Sakhatskyi, R. A. John, A. Guerrero, et al., "Assessing the Drawbacks and Benefits of Ion Migration in Lead Halide Perovskites," *ACS Energy Letters* 7 (2022): 3401–3414, https://doi.org/10.1021/acsenergylett.2c01663.

15. R. Kumar, M. Bag, and S. M. Jain, "Dual-Edged Sword of Ion Migration in Perovskite Materials for Simultaneous Energy Harvesting and Storage Application," *Iscience* 26 (2023): 108172, https://doi.org/10.1016/j.isci.2023.108172.

16. Z. Li, C. Xiao, Y. Yang, et al., "Extrinsic Ion Migration in Perovskite Solar Cells," *Energy & Environmental Science* 10 (2017): 1234–1242, https://doi.org/10.1039/C7EE00358G.

17. M. Saliba, T. Matsui, K. Domanski, et al., "Incorporation of Rubidium Cations Into Perovskite Solar Cells Improves Photovoltaic Performance," *Science* 354 (2016): 206–209, https://doi.org/10.1126/science.aah5557.

18. J. K. Nam, S. U. Chai, W. Cha, et al., "Potassium Incorporation for Enhanced Performance and Stability of Fully Inorganic Cesium Lead Halide Perovskite Solar Cells," *Nano Letters* 17 (2017): 2028–2033, https://doi.org/10.1021/acs.nanolett.7b00050.

19. L. Qiao, W.-H. Fang, R. Long, and O. V. Prezhdo, "Extending Carrier Lifetimes in Lead Halide Perovskites With Alkali Metals by Passivating and Eliminating Halide Interstitial Defects," *Angewandte Chemie* 132 (2020): 4714–4720, https://doi.org/10.1002/ange.201911615.

20. J. Cao, S. X. Tao, P. A. Bobbert, C. Wong, and N. Zhao, "Interstitial Occupancy by Extrinsic Alkali Cations in Perovskites and Its Impact on Ion Migration," *Advanced Materials* 30 (2018): 1707350, https://doi.org/10.1002/adma.201707350.

21. M. Abdi-Jalebi, Z. Andaji-Garmaroudi, S. Cacovich, et al., "Maximizing and Stabilizing Luminescence From Halide Perovskites With Potassium Passivation," *Nature* 555 (2018): 497–501, https://doi.org/10.1038/nature25989.

22. M. Abdi-Jalebi, Z. Andaji-Garmaroudi, A. J. Pearson, et al., "Potassium- and Rubidium-Passivated Alloyed Perovskite Films: Optoelectronic Properties and Moisture Stability," *ACS Energy Letters* 3 (2018): 2671–2678, https://doi.org/10.1021/acsenergylett.8b01504.

23. L. Kuai, Y. Wang, Z. Zhang, et al., "Passivating Crystal Boundaries With Potassium-Rich Phase in Organic Halide Perovskite," *Solar RRL* 3 (2019): 1900053, https://doi.org/10.1002/solr.201900053.

24. D. J. Kubicki, D. Prochowicz, A. Hofstetter, S. M. Zakeeruddin, M. Grätzel, and L. Emsley, "Phase Segregation in Cs-, Rb- and K-Doped Mixed-Cation $(MA)_x(FA)_{1-x}PbI_3$ Hybrid Perovskites from Solid-State NMR," *Journal of the American Chemical Society* 139 (2017): 14173–14180, https://doi.org/10.1021/jacs.7b07223.

25. J. M. Azpiroz, E. Mosconi, J. Bisquert, and F. De Angelis, "Defect Migration in Methylammonium Lead Iodide and Its Role in Perovskite Solar Cell Operation," *Energy & Environmental Science* 8 (2015): 2118–2127, https://doi.org/10.1039/C5EE01265A.

26. J. S. Yun, J. Seidel, J. Kim, et al., "Critical Role of Grain Boundaries for Ion Migration in Formamidinium and Methylammonium Lead Halide Perovskite Solar Cells," *Advanced Energy Materials* 6 (2016): 1600330, https://doi.org/10.1002/aenm.201600330.

27. Y. Shao, Y. Fang, T. Li, et al., "Grain Boundary Dominated Ion Migration in Polycrystalline Organic–Inorganic Halide Perovskite Films," *Energy & Environmental Science* 9 (2016): 1752–1759, https://doi.org/10.1039/C6EE00413J.

28. Y. Yang, J. Wu, X. Wang, et al., "Suppressing Vacancy Defects and Grain Boundaries via Ostwald Ripening for High-Performance and Stable

Perovskite Solar Cells," *Advanced Materials* 32 (2020): 1904347, https://doi.org/10.1002/adma.201904347.

29. Y. Zhao, I. Yavuz, M. Wang, et al., "Suppressing Ion Migration in Metal Halide Perovskite via Interstitial Doping With a Trace Amount of Multivalent Cations," *Nature Materials* 21 (2022): 1396–1402, https://doi.org/10.1038/s41563-022-01390-3.

30. N. Li, S. Tao, Y. Chen, et al., "Cation and Anion Immobilization Through Chemical Bonding Enhancement With Fluorides for Stable Halide Perovskite Solar Cells," *Nature Energy* 4 (2019): 408–415, https://doi.org/10.1038/s41560-019-0382-6.

31. W. Zhao, Z. Yao, F. Yu, D. Yang, and S. (Frank) Liu, "Alkali Metal Doping for Improved $CH_3NH_3PbI_3$ Perovskite Solar Cells," *Advanced Science* 5 (2018): 1700131, https://doi.org/10.1002/advs.201700131.

32. C. A. Aranda, A. O. Alvarez, V. S. Chivrony, C. Das, M. Rai, and M. Saliba, "Overcoming Ionic Migration in Perovskite Solar Cells Through Alkali Metals," *Joule* 8 (2024): 241–254, https://doi.org/10.1016/j.joule.2023.11.011.

33. S. Bai, P. Da, C. Li, et al., "Planar Perovskite Solar Cells With Long-Term Stability Using Ionic Liquid Additives," *Nature* 571 (2019): 245–250, https://doi.org/10.1038/s41586-019-1357-2.

34. B. Guo, R. Lai, S. Jiang, et al., "Ultrastable Near-Infrared Perovskite Light-Emitting Diodes," *Nature Photonics* 16 (2022): 637–643, https://doi.org/10.1038/s41566-022-01046-3.

35. C. Li, A. Guerrero, S. Huettner, and J. Bisquert, "Unravelling the Role of Vacancies in Lead Halide Perovskite Through Electrical Switching of Photoluminescence," *Nature Communications* 9 (2018): 5113, https://doi.org/10.1038/s41467-018-07571-6.

36. Y. Xi, G. Li, J. Jiao, T. Ji, Y. Hao, and Y. Cui, "2D Perovskite/Organic Heterojunction Black-Light Level Photodetector With Record-High Detectivity," *Advanced Functional Materials* 35 (2025): 2418614, https://doi.org/10.1002/adfm.202418614.

37. H. Xie, Q. Pan, D. Wu, et al., "Lateral Heterostructured Vis–NIR Photodetectors With Multimodal Detection for Rapid and Precise Classification of Glioma," *ACS Nano* 16 (2022): 16563–16573, https://doi.org/10.1021/acsnano.2c06004.

38. A. Liu, H. Zhu, S. Bai, et al., "High-Performance Metal Halide Perovskite Transistors," *Nature Electronics* 6 (2023): 559–571, https://doi.org/10.1038/s41928-023-01001-2.

39. W. Yu, F. Li, L. Yu, et al., "Single Crystal Hybrid Perovskite Field-Effect Transistors," *Nature Communications* 9 (2018): 5354, https://doi.org/10.1038/s41467-018-07706-9.

40. Z. Liu, P. Cheng, R. Kang, et al., "All-Inorganic $CsPbBr_3$ Perovskite Planar-Type Memristors as Optoelectronic Synapses," *ACS Applied Materials & Interfaces* 16 (2024): 51065–51079, https://doi.org/10.1021/acsami.4c09673.

41. J. Xing, C. Zhao, Y. Zou, et al., "Modulating the Optical and Electrical Properties of $MAPbBr_3$ Single Crystals via Voltage Regulation Engineering and Application in Memristors," *Light: Science & Applications* 9 (2020): 111, https://doi.org/10.1038/s41377-020-00349-w.

42. X. Xing, S. E. Ng, Y. B. Tay, N. Yantara, W. S. Lew, and N. Mathews, "Unravelling the Factors Influencing Halide Perovskite Based Switchable Photovoltaics," *Advanced Functional Materials* 34 (2024): 2315982, https://doi.org/10.1002/adfm.202315982.

43. W. Zhou, Y. Zhao, X. Zhou, et al., "Light-Independent Ionic Transport in Inorganic Perovskite and Ultrastable Cs-Based Perovskite Solar Cells," *The Journal of Physical Chemistry Letters* 8 (2017): 4122–4128, https://doi.org/10.1021/acs.jpclett.7b01851.

44. D. Moia, M. Jung, Y.-R. Wang, and J. Maier, "Ionic and Electronic Polarization Effects in Horizontal Hybrid Perovskite Device Structures Close to Equilibrium," *Physical Chemistry Chemical Physics* 25 (2023): 13335–13350, https://doi.org/10.1039/D3CP01182H.

45. R. A. Kerner, L. Zhao, S. P. Harvey, J. J. Berry, J. Schwartz, and B. P. Rand, "Low Threshold Voltages Electrochemically Drive Gold Migration in Halide Perovskite Devices," *ACS Energy Letters* 5 (2020): 3352–3356, https://doi.org/10.1021/acsenergylett.0c01805.

46. J. Pospisil, A. Guerrero, O. Zmeskal, et al., "Reversible Formation of Gold Halides in Single-Crystal Hybrid-Perovskite/Au Interface upon Biasing and Effect on Electronic Carrier Injection," *Advanced Functional Materials* 29 (2019): 1900881, https://doi.org/10.1002/adfm.201900881.

47. K. Domanski, J.-P. Correa-Baena, N. Mine, et al., "Not All That Glitters is Gold: Metal-Migration-Induced Degradation in Perovskite Solar Cells," *ACS Nano* 10 (2016): 6306–6314, https://doi.org/10.1021/acsnano.6b02613.

48. A. J. Knight, J. Borchert, R. D. J. Oliver, et al., "Halide Segregation in Mixed-Halide Perovskites: Influence of A-Site Cations," *ACS Energy Letters* 6 (2021): 799–808, https://doi.org/10.1021/acsenergylett.0c02475.

49. T. Jesper Jacobsson, J.-P. Correa-Baena, M. Pazoki, et al., "Exploration of the Compositional Space for Mixed Lead Halogen Perovskites for High Efficiency Solar Cells," *Energy & Environmental Science* 9 (2016): 1706–1724, https://doi.org/10.1039/C6EE00030D.

50. Y. Lin, Y. Shao, J. Dai, et al., "Metallic Surface Doping of Metal Halide Perovskites," *Nature Communications* 12 (2021): 7, https://doi.org/10.1038/s41467-020-20110-6.

51. H. Zhu, L. Pan, F. T. Eickemeyer, et al., "Efficient and Stable Large Bandgap MAPbBr 3 Perovskite Solar Cell Attaining an Open Circuit Voltage of 1.65 V," *ACS Energy Letters* 7 (2022): 1112–1119, https://doi.org/10.1021/acsenergylett.1c02431.

52. J. H. Heo, D. H. Song, and S. H. Im, "Planar $CH_3NH_3PbBr_3$ Hybrid Solar Cells With 10.4% Power Conversion Efficiency, Fabricated by Controlled Crystallization in the Spin-Coating Process," *Advanced Materials* 26 (2014): 8179–8183, https://doi.org/10.1002/adma.201403140.

53. M. Aebli, L. Piveteau, O. Nazarenko, et al., "Lead-Halide Scalar Couplings in ^{207}Pb NMR of $APbX_3$ Perovskites (A = Cs, Methylammonium, Formamidinium; X = Cl, Br, I)," *Scientific Reports* 10 (2020): 8229, https://doi.org/10.1038/s41598-020-65071-4.

54. B. A. Rosales, L. Men, S. D. Cady, M. P. Hanrahan, A. J. Rossini, and J. Vela, "Persistent Dopants and Phase Segregation in Organolead Mixed-Halide Perovskites," *Chemistry of Materials* 28 (2016): 6848–6859, https://doi.org/10.1021/acs.chemmater.6b01874.

55. Z. Fang, H. He, L. Gan, J. Li, and Z. Ye, "Understanding the Role of Lithium Doping in Reducing Nonradiative Loss in Lead Halide Perovskites," *Advanced Science* 5 (2018): 1800736, https://doi.org/10.1002/advs.201800736.

56. G. Y. Kim, A. Senocrate, Y.-R. Wang, D. Moia, and J. Maier, "Photo-Effect on Ion Transport in Mixed Cation and Halide Perovskites and Implications for Photo-Demixing**," *Angewandte Chemie International Edition* 60 (2021): 820–826, https://doi.org/10.1002/anie.202005853.

57. D. Shi, V. Adinolfi, R. Comin, et al., "Low Trap-State Density and Long Carrier Diffusion in Organolead Trihalide Perovskite Single Crystals," *Science* 347 (2015): 519–522, https://doi.org/10.1126/science.aaa2725.

58. Z. Xiao, Y. Yuan, Y. Shao, et al., "Giant Switchable Photovoltaic Effect in Organometal Trihalide Perovskite Devices," *Nature Materials* 14 (2015): 193–198, https://doi.org/10.1038/nmat4150.

59. D.-Y. Son, J.-W. Lee, Y. J. Choi, et al., "Self-Formed Grain Boundary Healing Layer for Highly Efficient $CH_3NH_3PbI_3$ Perovskite Solar Cells," *Nature Energy* 1 (2016): 16081, https://doi.org/10.1038/nenergy.2016.81.

60. P. Calado, A. M. Telford, D. Bryant, et al., "Evidence for Ion Migration in Hybrid Perovskite Solar Cells With Minimal Hysteresis," *Nature Communications* 7 (2016): 13831, https://doi.org/10.1038/ncomms13831.

61. Z. Fan, J. Xiao, K. Sun, et al., "Ferroelectricity of $CH_3NH_3PbI_3$ Perovskite," *The Journal of Physical Chemistry Letters* 6 (2015): 1155–1161, https://doi.org/10.1021/acs.jpclett.5b00389.

62. Y. Shao, Z. Xiao, C. Bi, Y. Yuan, and J. Huang, "Origin and Elimination of Photocurrent Hysteresis by Fullerene Passivation in $CH_3NH_3PbI_3$ Planar Heterojunction Solar Cells," *Nature Communications* 5 (2014): 5784, https://doi.org/10.1038/ncomms6784.

63. T. Leijtens, G. E. Eperon, A. J. Barker, et al., "Carrier Trapping and Recombination: The Role of Defect Physics in Enhancing the Open Circuit Voltage of Metal Halide Perovskite Solar Cells," *Energy & Environmental Science* 9 (2016): 3472–3481, https://doi.org/10.1039/C6EE01729K.

64. W. Tress, N. Marinova, T. Moehl, S. M. Zakeeruddin, M. K. Nazeeruddin, and M. Grätzel, "Understanding the Rate-Dependent J–V Hysteresis, Slow Time Component, and Aging in $CH_3NH_3PbI_3$ Perovskite Solar Cells: The Role of a Compensated Electric Field," *Energy & Environmental Science* 8 (2015): 995–1004, https://doi.org/10.1039/C4EE03664F.

65. C. Zhang, C. Liu, Y. Gao, et al., "Br Vacancy Defects Healed Perovskite Indoor Photovoltaic Modules With Certified Power Conversion Efficiency Exceeding 36%," *Advanced Science* 9 (2022): 2204138, https://doi.org/10.1002/advs.202204138.

66. M. H. Hebb, "Electrical Conductivity of Silver Sulfide," *The Journal of Chemical Physics* 20 (1952): 185–190, https://doi.org/10.1063/1.1700165.

67. G. Kresse and J. Furthmüller, "Efficiency of Ab-Initio Total Energy Calculations for Metals and Semiconductors Using a Plane-Wave Basis Set," *Computational Materials Science* 6 (1996): 15–50, https://doi.org/10.1016/0927-0256(96)00008-0.

68. G. Kresse and J. Furthmüller, "Efficient Iterative Schemes for Ab Initio Total-Energy Calculations Using a Plane-Wave Basis Set," *Physical Review B* 54 (1996): 11169–11186, https://doi.org/10.1103/PhysRevB.54.11169.

69. Y. Zhang and W. Yang, "Comment on "Generalized Gradient Approximation Made Simple"," *Physical Review Letters* 80 (1998): 890, https://doi.org/10.1103/PhysRevLett.80.890.

70. J. Neugebauer and M. Scheffler, "Adsorbate-Substrate and Adsorbate-Adsorbate Interactions of Na and K Adlayers on Al(111)," *Physical Review B* 46 (1992): 16067–16080, https://doi.org/10.1103/PhysRevB.46.16067.

71. H. J. Monkhorst and J. D. Pack, "Special Points for Brillouin-Zone Integrations," *Physical Review B* 13 (1976): 5188–5192, https://doi.org/10.1103/PhysRevB.13.5188.

72. S. Grimme, S. Ehrlich, and L. Goerigk, "Effect of the Damping Function in Dispersion Corrected Density Functional Theory," *Journal of Computational Chemistry* 32 (2011): 1456–1465, https://doi.org/10.1002/jcc.21759.

73. S. Grimme, J. Antony, S. Ehrlich, and H. Krieg, "A Consistent and Accurate ab Initio Parametrization of Density Functional Dispersion Correction (DFT-D) for the 94 Elements H-Pu," *The Journal of Chemical Physics* 132 (2010): 154104, https://doi.org/10.1063/1.3382344.

74. G. Henkelman, B. P. Uberuaga, and H. Jónsson, "A Climbing Image Nudged Elastic Band Method for Finding Saddle Points and Minimum Energy Paths," *The Journal of Chemical Physics* 113 (2000): 9901–9904, https://doi.org/10.1063/1.1329672.

75. G. Henkelman and H. Jónsson, "Improved Tangent Estimate in the Nudged Elastic Band Method for Finding Minimum Energy Paths and Saddle Points," *The Journal of Chemical Physics* 113 (2000): 9978–9985, https://doi.org/10.1063/1.1323224.

Supporting Information

Additional supporting information can be found online in the Supporting Information section.

Supporting File: aelm70540-sup-0001-SuppMat.docx.